

Parasitic Light Absorption, Rate Laws and Heterojunctions in the Photocatalytic Oxidation of Arsenic(III) Using Composite TiO₂/Fe₂O₃

Jay C. Bullen,^{*,[a, b, c]} Hany F. Heiba,^[a, b, c, d] Andreas Kafizas,^[b, e] and Dominik J. Weiss^{*,[a, f]}

Abstract: Composite photocatalyst-adsorbents such as TiO₂/Fe₂O₃ are promising materials for the one-step treatment of arsenite contaminated water. However, no previous study has investigated how coupling TiO₂ with Fe₂O₃ influences the photocatalytic oxidation of arsenic(III). Herein, we develop new hybrid experiment/modelling approaches to study light absorption, charge carrier behaviour and changes in the rate law of the TiO₂/Fe₂O₃ system, using UV-Vis spectroscopy, transient absorption spectroscopy (TAS), and kinetic analysis. Whilst coupling TiO₂ with Fe₂O₃ improves total arsenic removal by adsorption, oxidation rates significantly decrease (up to a factor of 60), primarily due to the parasitic absorption

of light by Fe₂O₃ (88% of photons at 368 nm) and secondly due to changes in the rate law from disguised zero-order kinetics to first-order kinetics. Charge transfer across this TiO₂-Fe₂O₃ heterojunction is not observed. Our study demonstrates the first application of a multi-adsorbate surface complexation model (SCM) towards describing As(III) oxidation kinetics which, unlike Langmuir-Hinshelwood kinetics, includes the competitive adsorption of As(V). We further highlight the importance of parasitic light absorption and catalyst fouling when designing heterogeneous photocatalysts for As(III) remediation.

Introduction

Arsenic is a carcinogen responsible for an estimated 30–40,000 deaths per year in Bangladesh alone,^[1] with tens of millions more people at risk.^[2] In the anoxic and reducing groundwaters of Bangladesh and West Bengal in India, arsenic is present as inorganic As(III) (*arsenite*), with the formula H₃AsO₃. Certain studies suggest that As(III) is up to 60 times more toxic than As(V)^[3] and, due to its neutral charge, As(III) is more difficult to remove than As(V) (*arsenate*, which is found as HAsO₄²⁻ and H₂AsO₄⁻ in oxic groundwaters).^[4] Adsorption onto iron oxides (with positive surface charge at neutral pH) is the preferred method for the removal of As(V).^[5] However, the removal of As(III) via adsorption is limited due to the competitive adsorption of oxyanions such as phosphate (PO₄³⁻) and sulfate (SO₄²⁻).^[6] This limits the lifetimes of arsenic filter devices, resulting in the failure of many arsenic mitigation schemes: replacing the sorbent media when saturated can be prohibitively expensive (exacerbated by the lack of market availability in rural communities) and users lack the confidence and know-how to regenerate the saturated sorbent media independently.^[7,8] Oxidation of As(III) to As(V) is therefore needed to increase adsorption capacity, improving filter device lifetimes for the more effective remediation of As(III).^[9]

The application of single-phase heterogeneous photocatalysts such as TiO₂ for the oxidation of As(III) has been explored over the past two decades.^[10] Unlike chemical oxidants such as chlorine, ozone and Fenton's reagent, heterogeneous photocatalysts are not associated with the risk of toxic disinfection by-products (DBPs) such as trihalomethanes (THM).^[11,12] (In fact, heterogeneous photocatalysts may play a role in the degradation of DBPs).^[13] Regardless of the approach towards oxidation,

[a] Dr. J. C. Bullen, H. F. Heiba, Prof. D. J. Weiss
Department of Earth Science and Engineering
Faculty of Engineering
Imperial College London
London SW7 2BX (UK)
E-mail: j.bullen16@imperial.ac.uk
d.weiss@imperial.ac.uk

[b] Dr. J. C. Bullen, H. F. Heiba, Dr. A. Kafizas
Department of Chemistry
White City Campus
Imperial College London
London W12 0BZ (UK)

[c] Dr. J. C. Bullen, H. F. Heiba
London Centre for Nanotechnology
London SW7 2AZ (UK)

[d] H. F. Heiba
Marine Chemistry Department
Environmental Division
National Institute of Oceanography and Fisheries (NIOF) (Egypt)

[e] Dr. A. Kafizas
The Grantham Institute
Faculty of Natural Sciences
Imperial College London
London SW7 2AZ (UK)

[f] Prof. D. J. Weiss
Civil and Environmental Engineering, E-Quad
Princeton University
Princeton (USA)

Supporting information for this article is available on the WWW under <https://doi.org/10.1002/chem.202104181>

© 2022 The Authors. Chemistry - A European Journal published by Wiley-VCH GmbH. This is an open access article under the terms of the Creative Commons Attribution License, which permits use, distribution and reproduction in any medium, provided the original work is properly cited.

a second step is required to remove the As(V) that is produced, for example adsorption or coprecipitation.

Coupling photocatalysts with an adsorbent material possessing affinity for the adsorption of As(V) is a promising strategy for the one-step remediation of As(III). This approach simplifies the oxidation-adsorption treatment, by using a single material in a single reactor, which may be advantageous given that many arsenic treatment plants fail due to maintenance issues.^[7,8,14,15] A variety of different composite photocatalyst-sorbent materials have been investigated.^[16–18] Titania (TiO₂) coupled with an iron oxide phase is the most popularly studied combination, since TiO₂ and iron oxides are benchmark materials for the photocatalytic oxidation of As(III) and adsorption of As(V) respectively. Examples include TiO₂ and iron oxide on slag iron,^[19] Fe₂O₃ on commercial TiO₂ powders,^[20] TiO₂/γ-Fe₂O₃ nanoparticles,^[21] TiO₂/Fe₂O₃ porous ceramic beads,^[22] TiO₂/Fe₃O₄ nanoparticles,^[23] and TiO₂/Fe₃O₄ nanosheets.^[24] Recent tertiary composites incorporating a conducting organic polymer with the aim of improving charge carrier separation include γ-Fe₂O₃/polyaniline/TiO₂,^[25] Fe₃O₄/polyparaphenylene diamine/TiO₂,^[26] and TiO₂/polythiophene/γ-Fe₂O₃.^[27]

Titania-iron oxide composites are stable and reusable: previous studies have used NaOH to regenerate TiO₂/Fe₂O₃ composites after the UV-assisted remediation of As(III), with efficiency decreasing by only 7.5% after 9 cycles,^[28] 12.5% after 5 cycles,^[21] and 20% after 5 cycles.^[22] Elsewhere, dissolution studies have shown that in the dark < 8 μg L⁻¹ TiO₂ is dissolved after one month of immersion at pH 3 (40 m² L⁻¹ TiO₂)^[29] and < 0.24 mg L⁻¹ Fe₂O₃ is dissolved after 20 h of immersion at pH 2.4 (5 g L⁻¹ Fe₂O₃).^[30] The reductive dissolution of iron oxides is promoted under ultraviolet illumination, but only at acidic pH (e.g. pH 3) and in the presence of Fe(II) complexing ligands,^[31,32] conditions neither present in our experimental work nor in naturally occurring As(III)-contaminated groundwaters.^[33–35]

Despite significant research activity into these materials, no previous study has investigated how the photocatalytic oxidation of As(III) is affected when the TiO₂ photocatalyst is coupled to an iron oxide sorbent phase (e.g. Fe₂O₃). For instance, no study has considered how the rate equation might change and the reasons why. Although iron oxides are established adsorbents for arsenic remediation,^[36] as single-phase materials they are typically poor photocatalysts due to fast electron-hole recombination kinetics^[37] and show negligible activity towards the oxidation of As(III).^[18] In composite photocatalysts, incorporation of an iron oxide phase may improve photocatalytic activity beyond the sum of its parts due to charge carrier transfer across the semiconductor heterojunction (which improves charge carrier lifetimes by reducing electron-hole recombination rates).^[38,39] Alternatively, iron oxide phases may reduce reaction rates due to the parasitic absorption of incident photons, suppressing the photoexcitation of TiO₂.^[40] There is also evidence that sorbent-coupling prevents photocatalyst deactivation (catalyst fouling).^[41] Given the potential for iron oxides to both enhance and suppress TiO₂ photocatalytic oxidation rates, it is essential to characterize the mechanisms by which material coupling influences the photocatalytic oxidation

of As(III), to engineer effective treatments using these new composite photocatalyst-sorbent materials. To date, no previous study has investigated the influence of parasitic absorption, charge transfer across the heterojunction, or changes to the rate law in the photocatalytic oxidation of As(III) using titania-iron oxide composite photocatalysts.^[28,42–44]

We previously developed new adsorption models for TiO₂/Fe₂O₃ composites, showing how the monolayer adsorption of As(V) onto TiO₂/Fe₂O₃ obeys component additivity, i.e. the reaction proceeds as adsorption onto non-interacting TiO₂ and Fe₂O₃ surface components, unaffected when TiO₂ and Fe₂O₃ are coupled into a composite structure.^[45] In contrast, As(III) adsorption is not component additive when there are differences between the morphology of (i) the TiO₂/Fe₂O₃ composite and (ii) the single-component TiO₂ and Fe₂O₃ reference samples, since surface morphology influences the extent of multilayer As(III) adsorption. We also developed a kinetic adsorption model to explore how a treatment based upon simultaneous photocatalytic oxidation-adsorption using TiO₂/Fe₂O₃ would be best designed, finding that high concentrations of the media (compared with photocatalysis-only reactors) are required to achieve sufficient sorbent lifetimes.^[46]

Having previously established the adsorption mechanisms, the aim of the present study was to understand the photocatalytic oxidation of As(III) using TiO₂/Fe₂O₃ composites, determining for the first time how coupling TiO₂ with an Fe₂O₃ sorbent phase affects the photocatalytic oxidation of As(III), considering both the reaction kinetics and mechanisms. To this end, new hybrid experimental-modelling approaches were developed.

We first synthesized and characterized TiO₂ and TiO₂/Fe₂O₃ photocatalysts, using the synthesis procedure described by Zhou et al.^[28] without further optimization, as an example of the typical TiO₂/Fe₂O₃ composites prepared by precipitation to produce discrete TiO₂ and Fe₂O₃ phases.^[20,22,38,42,45,46] Previous studies of TiO₂/Fe₂O₃ composites have only considered arsenic removal at high As concentrations and/or in blank media.^[19–21,28,45] We thus verify that coupling TiO₂ with the Fe₂O₃ sorbent phase truly improves total arsenic removal under environmentally relevant conditions (the groundwaters in South Asia rarely exceed 1 mg L⁻¹ arsenic,^[47] i.e. lower concentrations than those under which composite photocatalysts have been previously tested,^[24,28] and these waters are typically rich in competitor ions such as phosphate).^[33]

Secondly, we studied the key mechanisms by which coupling TiO₂ with Fe₂O₃ might influence the photocatalytic oxidation of As(III), i.e. parasitic absorption of ultraviolet light by Fe₂O₃, enhanced charge carrier separation across the TiO₂–Fe₂O₃ heterojunction, and photocatalyst deactivation. We determined the extent of parasitic absorption using UV-Vis spectroscopy and component additivity (the linear combination of experimental data collected using single-phase TiO₂ and Fe₂O₃ reference samples^[45]). We then developed a new model to predict transient absorption spectroscopy (TAS) decay kinetics using component additivity and evaluate the extent of charge transfer across the heterojunction. We thus establish, for the first time, a mechanistic explanation for the differences in

As(III) oxidation kinetics observed after mesoporous TiO₂ is coupled with Fe₂O₃.

Thirdly, we determined the kinetic rate laws governing As(III) oxidation using meso-TiO₂ and meso-TiO₂/Fe₂O₃ photocatalysts, developing new models to reconcile the results of initial rates analysis with data at later times. Previous studies have been limited to modelling the photocatalytic oxidation of As(III) using zero-order,^[48] pseudo-first order (PFO)^[49,50] and Langmuir-Hinshelwood (LH) kinetics.^[51,52] Due to the capability of adsorbed As(V) to deactivate TiO₂^[41] we developed new kinetic models constrained using the multi-surface, multi-sorbate surface complexation model (SCM) reported in our previous work,^[45] incorporating the competitive adsorption of As(V) and As(III) into a model of oxidation kinetics for the first time. We performed these kinetic experiments at pH 7.3 ± 0.1, representing As(III) contaminated waters in South Asia.^[33–35]

Results and Discussion

Materials characterisation

The synthesised meso-TiO₂ was off-white in colour. Fe₂O₃ and the meso-TiO₂/Fe₂O₃ composite were both red, with Fe₂O₃ being darker in color than the composite.

XRD patterns are provided in Supporting Information Figure S3, revealing the presence of both anatase (*I4₁/amd*) and rutile (*P4₂/mnm*) crystal phases of TiO₂. Application of the Spurr and Myers equation^[53] indicates that anatase was the dominant phase of TiO₂ (~84% anatase and ~16% rutile by mass in meso-TiO₂, and ~86% anatase, ~14% rutile in meso-TiO₂/Fe₂O₃). Hematite (α -Fe₂O₃, *R-3cH*) was the only crystalline iron oxide phase identified. Application of the Scherrer equation to the XRD pattern of meso-TiO₂ gave average crystallite diameters of 10.0 ± 0.4 nm for the anatase component and 16.8 ± 2.5 nm for the rutile component.

For meso-TiO₂/Fe₂O₃, average crystallite diameters of 13 ± 2.1 nm were observed for the anatase component, 16 ± 3.5 nm for the rutile component, and 18.5 ± 3.1 nm for the Fe₂O₃ component. This agrees with transmission electron microscopy (TEM) analysis (Supporting Information Figure S4). Crystallites were largest in the Fe₂O₃ reference sample, with an average diameter of 20.5 ± 5 nm. Scanning electron microscopy (SEM) indicated that the crystallites of meso-TiO₂ and meso-TiO₂/Fe₂O₃ were aggregated into larger particles between ~0.5 and 50 μm in size (Supporting Information Figure S5). In contrast, the Fe₂O₃ reference sample was coarser, with many particles being up to 100 μm in size.

Using meso-TiO₂ and Fe₂O₃ as end-member reference samples, XRF analysis indicated that meso-TiO₂/Fe₂O₃ was 44.4 ± 2.4% meso-TiO₂ and 55.6 ± 3.0% Fe₂O₃ by mass (section Supporting Information 2.4). This is close to the theoretical 50:50 mass ratio based upon the quantity of reagents used during synthesis. The BET-specific surface areas of meso-TiO₂, meso-TiO₂/Fe₂O₃ and Fe₂O₃ were 146, 116, and 103 m²g⁻¹ respectively, and the average pore sizes were 8.9, 8.8 and

11.1 nm, as determined from the BJH analysis of N₂ adsorption-desorption isotherms (Supporting Information Figures S8–9).

We also previously characterized meso-TiO₂/Fe₂O₃ using scanning transmission electron microscopy energy-dispersive X-ray spectroscopy (STEM-EDS), finding that the Fe₂O₃ phase of meso-TiO₂/Fe₂O₃ is present both as a thin surface coating (i.e. < 10 nm thickness) and as more discrete surface-bound nanoparticle structures.^[45] Low energy ion scattering (LEIS) revealed that Fe₂O₃ covered 68 ± 1% of the surface, whilst only 32 ± 1% was TiO₂.

Previous analysis of the near-surface using X-ray photoelectron spectroscopy (XPS) showed Ti(IV) with binding energies of 459.14 and 464.90 eV for Ti2p_{3/2} and Ti2p_{1/2} respectively and Fe(III) with binding energies of 711.46 and 724.81 eV for Fe2p_{3/2} and Fe2p_{1/2} respectively.^[45] No other oxidation states were found for these transition metals (i.e. no Fe(II) with Fe2p_{3/2} at 722.6 eV and Fe2p_{1/2} at 709.0 eV)^[54] in agreement with characterization of the bulk material using XRD.

Improved total arsenic removal under environmental conditions using the composite photocatalyst-adsorbent approach for a one-step treatment

Under environmentally relevant conditions (1 mg L⁻¹ total As, and with 10 mg L⁻¹ phosphate or in natural groundwater) (1) photocatalytic oxidation significantly improves total arsenic removal, and (2) addition of the Fe₂O₃ sorbent phase to the meso-TiO₂ photocatalyst improves total arsenic removal (Figure 1). These effects are cumulative. We previously found that the adsorption capacity of meso-TiO₂/Fe₂O₃ is comparable with

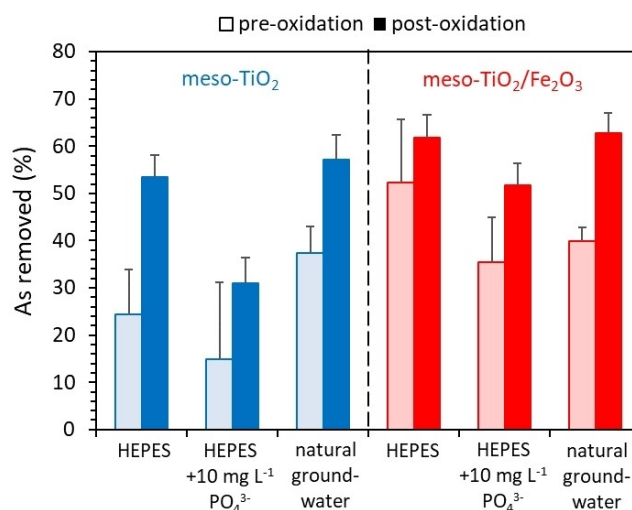


Figure 1. Comparison of total arsenic removal before (light bars) and after (dark bars) photooxidation, using meso-TiO₂ (blue) and meso-TiO₂/Fe₂O₃ (red) photocatalysts in a variety of media. The experimental conditions were 1 mg L⁻¹ initial As(III) (adsorbed in the dark overnight), 0.1 g L⁻¹ catalyst loading, pH 7.3 ± 0.1. Meso-TiO₂ suspensions were irradiated for a minimum of 30 minutes, and meso-TiO₂/Fe₂O₃ suspensions for a minimum of 120 minutes, after which < 20 μg L⁻¹ aqueous As(III) remained (i.e. ≥ 98% oxidation). Error bars indicate the uncertainty calculated from the standard error between 2 and 3 repeat ASV measurements.

that of the commercial goethite (FeOOH) sorbent *Bayoxide E33*.^[45] These increases in total arsenic removal highlight the potential for the composite photocatalyst-sorbent system to improve As(III) remediation by combining oxidation capabilities with high As(V) adsorption capacities in a single-step treatment.

Quantifying parasitic light absorption by Fe₂O₃ using UV-Vis spectroscopy and component additivity

The UV-Vis absorption spectra of powders suspended in water are presented in Figure 2a. Fe₂O₃ shows a characteristic absorption band edge from 600 nm to lower wavelengths. Meso-TiO₂ shows a sharper band edge, characteristic of this material, from around 380 nm to lower wavelengths. The UV-Vis absorbance spectra of meso-TiO₂/Fe₂O₃ is dominated by the influence of Fe₂O₃. The single-component Fe₂O₃ sample shows a broad absorption from 600 nm to 1200 nm due to residual scattering not captured by the integrating sphere. This scattering is not present in the other samples and indicates that

larger particles are present in the Fe₂O₃ sample^[55] in agreement with SEM and DLS analysis.^[45]

The bandgaps of meso-TiO₂, meso-TiO₂/Fe₂O₃ and Fe₂O₃ powder samples were estimated using a Tauc plot.^[56] As absorption could not be determined from the dry powders, F(R), a parameter that is proportional to the extinction coefficient, was determined from diffuse reflectance data using the Kubelka-Munk function.^[57] An exponential power of 1/2 was used in the Tauc plot given that anatase TiO₂ has an indirect allowed bandgap^[58] whilst Fe₂O₃ shows both direct and indirect transitions at nearly equivalent energies.^[59] The bandgap of the majority anatase phase within meso-TiO₂ is 3.2 eV, though a weaker absorbance corresponding to the minority rutile phase is also seen at 3.0 eV (Figure 2b) (cf. literature values of 3.03 and 3.20 eV respectively).^[60] The only bandgap that can be identified in the Tauc plot of composite meso-TiO₂/Fe₂O₃ is that of Fe₂O₃ at 2.0 eV (cf. literature values of 1.9–2.2 eV).^[61]

A linear combination of the UV-Vis absorbance spectra recorded for meso-TiO₂ and Fe₂O₃ [weighted 44% and 56% respectively as per XRF analysis, Equation (2)] successfully predicts the absorbance curve and extinction coefficient of meso-TiO₂/Fe₂O₃ at wavelengths shorter than 540 nm (Figure 2a), suggesting component additivity. Using Equation (3), the component additive prediction of the absorption coefficient ϵ is 2.2 g⁻¹ cm⁻¹ for meso-TiO₂/Fe₂O₃ (at λ = 368 nm and 0.1 g L⁻¹), which is marginally greater than the experimentally observed 2.0 g⁻¹ cm⁻¹. The ultraviolet absorption of composite meso-TiO₂/Fe₂O₃ can therefore be treated as the mass-weighted linear combination of non-interacting meso-TiO₂ and Fe₂O₃ components.

Using Equation (4), component additivity predicts that only 12% of incident photons are absorbed by the meso-TiO₂ component at λ = 368 nm (the wavelength of the UV lamp used in our photocatalysis experiments). The remaining 88% of incident photons are absorbed by the Fe₂O₃ component. This is an important finding, given that (a) single-component Fe₂O₃ shows negligible activity towards the photocatalytic oxidation of As(III) compared with TiO₂^[18] and (b) the transfer of charge carriers from Fe₂O₃ to TiO₂ is energetically unfavourable (see following section). The Fe₂O₃ phase is therefore anticipated to parasitically absorb the majority of incident light without promoting the oxidation of As(III). To the author's knowledge, this is the first time that the simple approach of mass-weighted component additivity has been used to approximate parasitic light absorption within composite photocatalysts for As(III) oxidation.

Identifying the role of the TiO₂/Fe₂O₃ heterojunction using transient absorption spectroscopy (TAS) and component additivity

The conduction band of anatase TiO₂ is more negative than that of Fe₂O₃ (ca. -0.3 eV versus ca. +0.3 eV) whilst the valence band of anatase TiO₂ is more positive than that of Fe₂O₃ (ca. +2.9 eV versus ca. +2.5 eV).^[62] As shown in Figure 3, these crystal phases form a straddling gap (type-I) heterojunction,

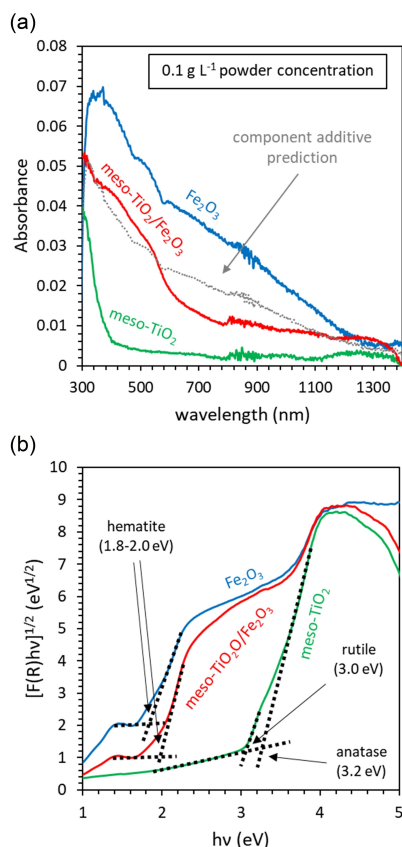


Figure 2. UV-Vis spectroscopy used to evaluate parasitic light absorption. (a) UV-Vis absorbance of meso-TiO₂, meso-TiO₂/Fe₂O₃, and Fe₂O₃ powders (0.1 g L⁻¹, suspended in Milli-Q water). The dashed grey-line indicates the component additive prediction (using the meso-TiO₂ and Fe₂O₃ spectra as end-members, weighted according to the XRF mass ratio). The path length was 2 mm. (b) Bandgap determination using diffuse reflectance spectra of dry powders (converted to F(R) using the Kubelka-Munk function). The bandgap was identified by extrapolating the steep linear regions of the Tauc plot to where the background absorption is intercepted.

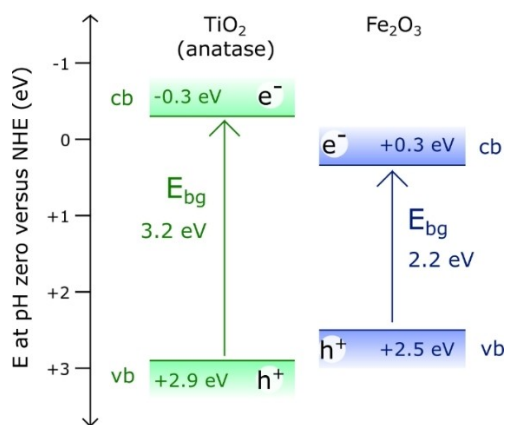


Figure 3. Band alignment of the anatase TiO_2 and hematite Fe_2O_3 phases within the meso- $\text{TiO}_2/\text{Fe}_2\text{O}_3$ composite photocatalyst. Band energies are from the literature.^[64]

wherein the transfer of both electrons and holes from TiO_2 to Fe_2O_3 is thermodynamically favourable.^[63] It was therefore important to assess whether charge transfer across the heterojunction of meso- $\text{TiO}_2/\text{Fe}_2\text{O}_3$ does indeed occur, given the potential enhancement in photocatalytic activity that this effect can generate.^[64]

Typical transient absorption decays for meso- TiO_2 , Fe_2O_3 and the meso- $\text{TiO}_2/\text{Fe}_2\text{O}_3$ composite are presented in Figure 4a, with the full spectrum of wavelengths presented in Supporting Information Figure S23. Assuming component additivity, the product of the optical density and mass fraction of each component [Eq. (4)] estimates that 37% of the absorbed laser pulse is absorbed by the meso- TiO_2 component, and that the remaining 63% is absorbed by Fe_2O_3 .

The linear combination of normalized transient absorption decays, weighted according to these results [Eq. (8)], closely predicts the experimentally observed transient absorption decay of meso- $\text{TiO}_2/\text{Fe}_2\text{O}_3$ across all wavelengths (Figure 4b). The charge carrier life-times within meso- $\text{TiO}_2/\text{Fe}_2\text{O}_3$ (as a dry powder) are therefore no different than the life-times expected for a mixture of non-interacting meso- TiO_2 and Fe_2O_3 powders. This indicates that despite there being a thermodynamic driving force for the charge carriers formed in meso- TiO_2 to transfer into Fe_2O_3 and spatially separate (Figure 3), meso- $\text{TiO}_2/\text{Fe}_2\text{O}_3$ charge carrier lifetimes are no longer than those of single-component meso- TiO_2 and Fe_2O_3 parent materials. Consequently, the TiO_2 - Fe_2O_3 heterojunction within meso- $\text{TiO}_2/\text{Fe}_2\text{O}_3$ is not expected to improve photocatalytic activity. This is attributed to (i) the high parasitic absorption of light by Fe_2O_3 (~63%), whose charge carriers must overcome a high thermodynamic barrier to transfer into meso- TiO_2 and spatially separate, and (ii) limited interfacial contact between Fe_2O_3 and TiO_2 phases, as indicated by our SEM images (Supporting Information Figure S5).

Whilst the charge carrier life times of titania-iron oxide composites have been previously studied and modelled using TAS,^[65] to our knowledge, this is the first time that the component additive prediction of charge carrier lifetimes using

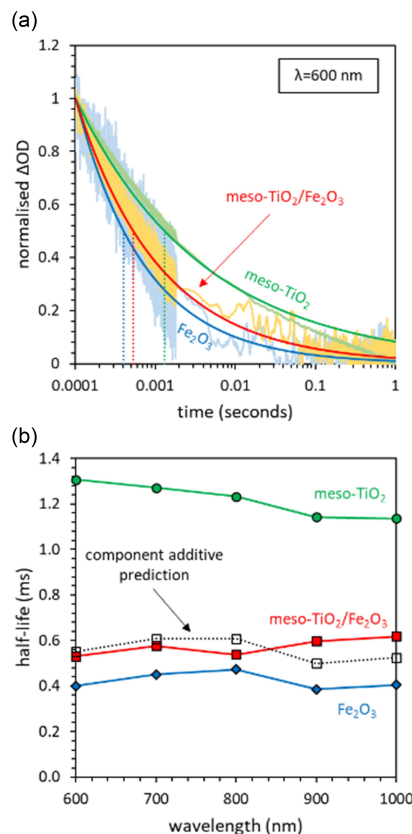


Figure 4. Identifying the role of the heterojunction formed in the composite meso- $\text{TiO}_2/\text{Fe}_2\text{O}_3$ photocatalyst using transient absorption spectroscopy (TAS) to probe charge carrier lifetimes. (a) Transient decay kinetics (with an example shown for the 600 nm probe) showed power-law decays in all materials and at all probe wavelengths ($\lambda = 600$ –1000 nm), (b) A comparison of the transient absorption half-lives observed experimentally with the half-lives of meso- $\text{TiO}_2/\text{Fe}_2\text{O}_3$ predicted by component additivity (using meso- TiO_2 and Fe_2O_3 as end-member reference samples).

single-component reference samples has been used to identify the role of the heterojunction.

Photocatalytic oxidation kinetics and the effect of coupling TiO_2 with Fe_2O_3

The influence of light intensity on the initial rate of As(III) photocatalytic oxidation

Single-component meso- TiO_2 and composite meso- $\text{TiO}_2/\text{Fe}_2\text{O}_3$ show different responses to changes in light intensity (Figure 5). A linear relationship between light intensity and the initial rate of As(III) oxidation is observed for meso- $\text{TiO}_2/\text{Fe}_2\text{O}_3$. In contrast, the meso- TiO_2 system initially shows a first-order relationship between light intensity and the initial rate between 0 and 2.5 mW cm^{-2} , after which the initial rate becomes independent of light intensity. Whilst this typically indicates mass transport limitations, we find that the As(III) concentration has no effect upon the initial rate (see following section). It therefore remains unclear whether the zero-order relationship after 2.5 mW cm^{-2}

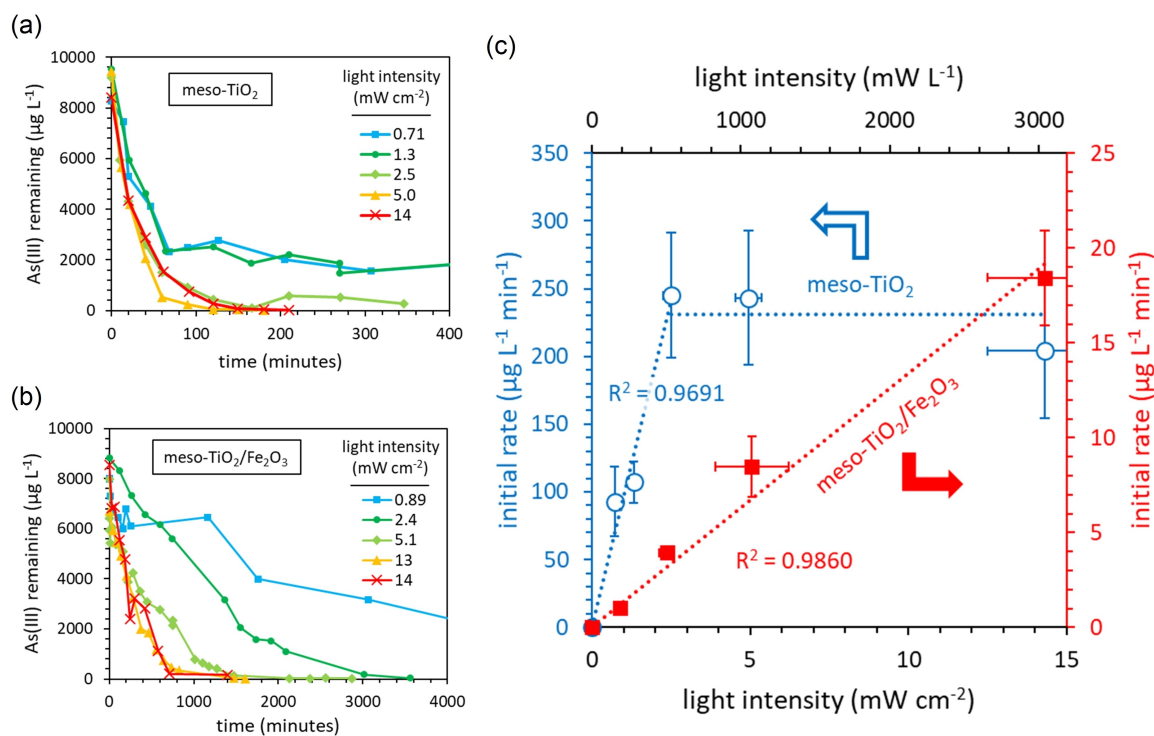


Figure 5. The influence of light intensity on the initial rate of As(III) photocatalytic oxidation in the presence of meso-TiO₂ and meso-TiO₂/Fe₂O₃ photocatalysts. The light intensity was varied by increasing and decreasing the distance between the UV lamp ($\lambda = 368$ nm) and the photoreactor surface. The experimental conditions were 10 mg L⁻¹ initial As(III), 0.1 g L⁻¹ photocatalyst, 10 mM HEPES (pH 7.3 ± 0.1), 14 mW cm⁻² light intensity ($\lambda = 368$ nm) and 100 mL total volume. Error bars indicate the standard deviation in the slope of the linear regression used to calculate initial rates. The average uncertainty in the calculated concentration of As(III) is 10%.

is due to increased electron-hole recombination or mass transport limitations. Similar results were observed by Dutta et al. (using 0.1 g L⁻¹ Degussa P25 TiO₂), with the slope of reaction rate as a function of light intensity decreasing at 6 mW cm⁻².^[48] Dutta et al. found that overall the rate of reaction was proportional to $I^{0.23}$, where I is the light intensity, raising possibilities of both increased electron-hole recombination and mass transport limitations at high light intensity.

The oxidation of As(III) did not reach completion when using meso-TiO₂ at the lowest light intensities (0.71–1.3 mW cm⁻²). This could be a result of photocatalyst deactivation caused by the adsorption of As(V), as explored later. In contrast, all reactions proceeded to completion when using meso-TiO₂/Fe₂O₃, suggesting that the presence of a sorbent phase prevents catalyst deactivation, as proposed by Vaiano et al.^[66] The quantum yield (Φ) indicates the number of reactions completed per incident photon. At 2.5 mW cm⁻² light intensity, the quantum yield of As(III) oxidation is greater when using meso-TiO₂ than when using meso-TiO₂/Fe₂O₃, with a 68 times difference ($\Phi = 3.9 \pm 0.9\%$ versus $\Phi = 0.057 \pm 0.017\%$ respectively). As light intensity is increased beyond 2.5 mW cm⁻², this difference in quantum efficiency decreases: the quantum yield of meso-TiO₂ decreases with increasing light intensity ($\Phi = 0.57 \pm 0.6\%$ at 14.3 mW cm⁻²) whilst the quantum yield of meso-TiO₂/Fe₂O₃ is maintained ($\Phi = 0.051 \pm 0.010\%$ at 14.0 mW cm⁻²). UV-Vis absorption spectroscopy shows that due to parasitic absorption by Fe₂O₃, the meso-TiO₂ component of

the composite photocatalyst only absorbs 12% of the total ultraviolet photons. Consequently, the relative rate of electron-hole recombination within the TiO₂ phase of meso-TiO₂/Fe₂O₃ at 14 mW cm⁻² is theoretically equivalent to that of meso-TiO₂ with just 1.7 mW cm⁻², which is within the linear range of initial rates versus light intensity. The linear relationship between light intensity and the initial reaction rate therefore extends to higher values of light intensity for the composite photocatalyst than pure meso-TiO₂, due to parasitic light absorption.

The difference in oxidation rates is too great to be explained by parasitic light absorption alone (discussed in detail later). We consequently investigated the kinetic mechanisms of both photocatalyst systems to identify whether Fe₂O₃-coupling affects the reaction pathway of As(III) photooxidation. Initial rates were used to determine the order of reaction, and data at later times was then used to understand the role of As(V) catalyst deactivation and adsorption-controlled kinetics.

The reaction order determined from initial rates

Meso-TiO₂ and meso-TiO₂/Fe₂O₃ responded differently to changes in the concentration of As(III) (Figure 6). In the presence of meso-TiO₂, the initial rate was independent of the As(III) concentration (0.5–10 mg L⁻¹ As(III) added). Zero-order kinetics were also observed by Dutta et al. using TiO₂.^[48] Zero-order kinetics can be caused by saturation of the catalyst

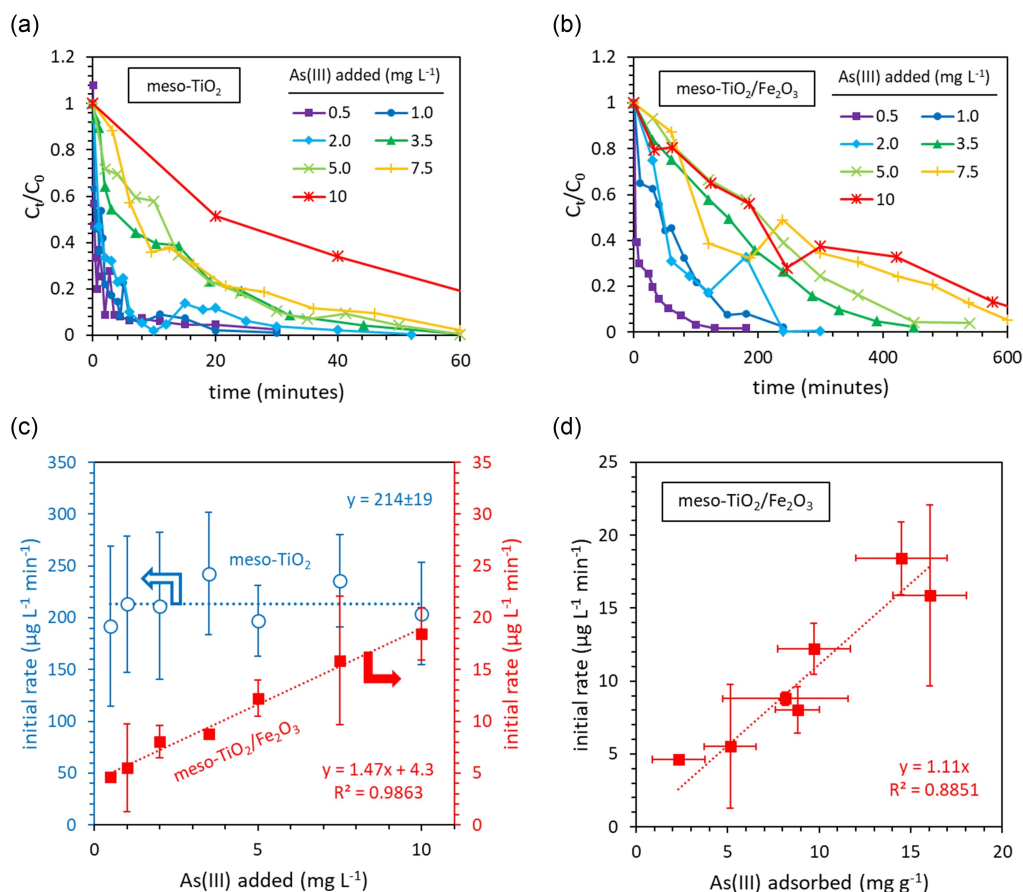


Figure 6. The influence of initial As(III) concentrations on photocatalytic oxidation kinetics in the presence of (a) meso-TiO₂ and (b) meso-TiO₂/Fe₂O₃ photocatalysts. (c) The influence of As(III) concentration on the initial rate. (d) The influence of adsorbed As(III) on the initial rate. The experimental conditions were 0.5–10 mg L⁻¹ As(III), 0.1 g L⁻¹ photocatalyst, 10 mM HEPES (pH 7.3 ± 0.1), 14 mW cm⁻² light intensity (λ = 368 nm), and 100 mL total volume. Error bars indicate the uncertainty in the initial rate determined as the standard deviation of the slope in the linear regression fitted to the initial experimental kinetics. The average uncertainty in the calculated concentration of As(III) was 10%.

surface.^[67] However, our previous work found that at pH 7.0 ± 0.1, monolayer coverage is incomplete when [As(III) (aq)] < 10 mg L⁻¹^[45] as per this study. Consequently, the observed zero-order kinetics indicate that the rate determining step is linked to another process, such as the generation of holes, electrons or reactive oxygen species (ROS) intermediates.^[67] Phosphate can suppress photocatalysis reaction rates through competitive adsorption and surface-site blocking, or enhance rates through the promotion of hydroxyl radical formation.^[40] The addition of phosphate increased meso-TiO₂ reaction rates and did not interfere with the charge scavenging behaviour of As(III) (Supporting Information Figure S14) suggesting that the rate is determined by the production of ROS, and not the availability of As(III).^[40]

For meso-TiO₂/Fe₂O₃, a linear relationship is observed between the initial rate and the concentration of As(III) (Figure 6c). This relationship is imperfect due to an offset from the origin by a positive y-intercept. Consequently, the system approximates pseudo-first order (PFO) kinetics at high As(III) concentrations. In contrast, the first-order relationship observed between the initial rate and the concentration of adsorbed As(III) is valid even at low As(III) concentrations (Figure 6d). This

indicates that unlike meso-TiO₂, adsorbed As(III) is involved in the rate determining step when using meso-TiO₂/Fe₂O₃. The addition of phosphate (a) decreases As(III) adsorption and (b) suppresses reaction rates (Supporting Information Figure S14), providing further evidence that the kinetics of meso-TiO₂/Fe₂O₃ are controlled by the concentration of adsorbed As(III).^[40]

Kinetic data at later times

Whilst initial rates established a zero-order relationship between the concentration of As(III) and meso-TiO₂ photocatalytic oxidation kinetics (see previous section), the data at later times cannot be described by the zero-order kinetic model as in all cases the reaction rate slows as As(III) is depleted, being best fit using a pseudo-first order (PFO) kinetic model (Figure 7a). The combined analysis of initial rates and data at later times reveals that meso-TiO₂ follows disguised zero-order kinetics.^[67]

When using meso-TiO₂/Fe₂O₃, data at later times also disagrees with the analysis of initial rates. PFO linearization is successful when less than 2 mg L⁻¹ As(III) is added (Figure 7b). However, linearization fails with more than 2 mg L⁻¹ As(III), since

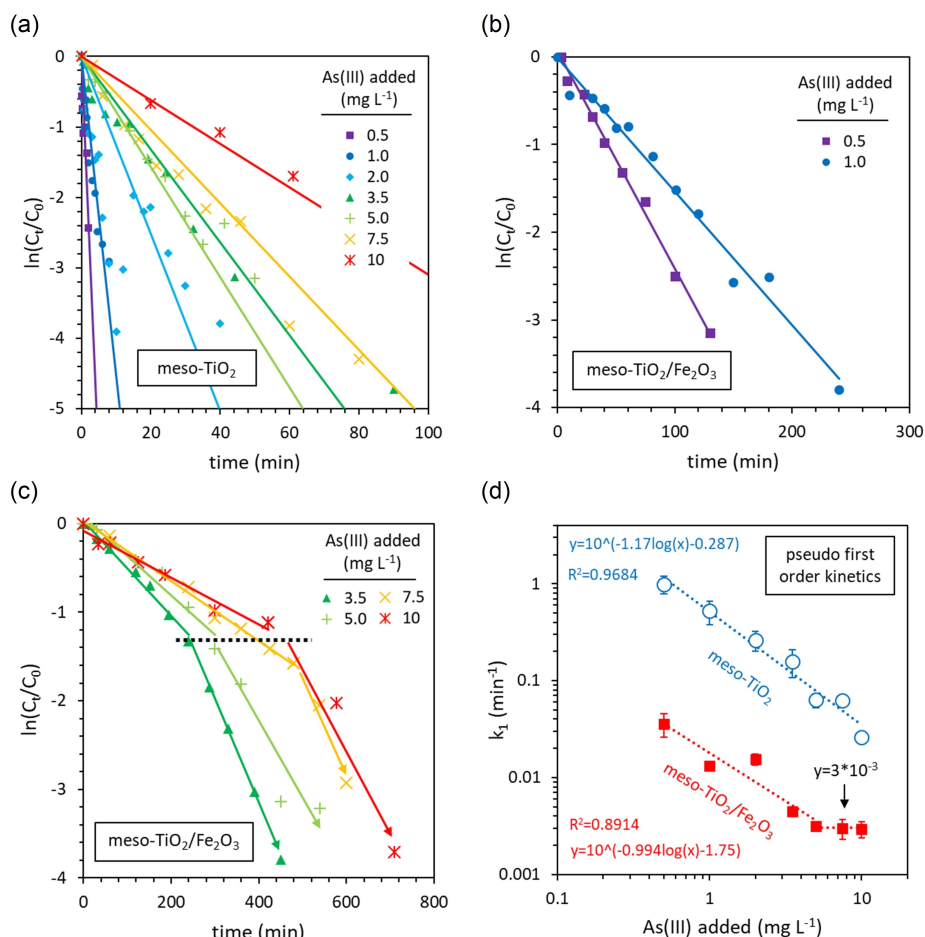


Figure 7. Linearisation of data at later times using pseudo first-order kinetics. The successful linearisation of (a) meso-TiO₂, and (b) meso-TiO₂/Fe₂O₃ with 0.5 and 1 mg L⁻¹ initial As(III). (c) The failed linearisation of meso-TiO₂/Fe₂O₃ data with ≥ 3.5 mg L⁻¹ As(III). (d) The influence of As(III) concentrations on the PFO rate constant, k_1 . All values of k_1 were calculated from the initial linear region of $\ln(C_t/C_0)$ versus time. The average R^2 values of the linear regression of the PFO plots were 0.9327 ± 0.075 for meso-TiO₂ and 0.9747 ± 0.0297 for initial linear region for meso-TiO₂/Fe₂O₃.

the slope of $\ln(C_t/C_0)$ versus time increases in magnitude when $\ln(C_t/C_0) \approx -1.5$ (Figure 7c). This contradicts the analysis of initial rates which suggests that PFO kinetics should be best approximated at higher As(III) concentrations, rather than at low As(III) concentrations. The curvature in $\ln(C_t/C_0)$ as a function of time can also be observed in the study of Ferguson et al. (3.2 mg L⁻¹ initial As(III) and Degussa P25 TiO₂).^[50] In their study, no curvature was observed at lower initial As(III) concentrations of 0.19 mg L⁻¹, similar to our results.

The influence of the As(III) concentration on the PFO rate constant (k_1) is presented in Figure 7d. For meso-TiO₂, k_1 decreases exponentially with increasing As(III) concentrations, in-line with disguised zero-order kinetics.^[67] For meso-TiO₂/Fe₂O₃, k_1 decreases exponentially as the As(III) concentration is increased, up to 5 mg L⁻¹, whereupon k_1 stabilizes. With a stable k_1 at high As(III) concentrations, this trend contradicts the failure of PFO kinetics to linearize data at later times (Figure 7c) but agrees with the analysis of initial rates in the previous section.

The following discussion reconciles data at later times with initial rates analysis by developing new rate equations to

provide rate constants that are consistent across the 0.5–10 mg L⁻¹ As(III) concentration range.

Disguised zero-order kinetics of meso-TiO₂ explained by photocatalyst deactivation

The method of initial rates is widely considered to reveal the true reaction order, whilst data at later times can ‘disguise’ the true rate law.^[67] The true rate law will satisfy two conditions: (1) the initial rate is not influenced by the concentration of As(III), and (2) the absolute reaction rate decreases as oxidation progresses. Vaiano et al. reported deactivation of TiO₂ due to the adsorption of As(V), reducing photocatalytic activity.^[41] We similarly identified incomplete oxidation of As(III) using meso-TiO₂ with low light intensities (Figure 5a). We therefore considered deactivation of meso-TiO₂ due to the presence of As(V) as an explanation for disguised zero-order kinetics.

We developed and explored two new rate equations that depend upon the concentration of As(V). The first model uses C_0 and C_t parameters, i.e. aqueous phase parameters only. This

model is presented and discussed in Supporting Information section 6 and goes some way towards reconciling initial rates and data at later times (Supporting Information Figure S19). However, photocatalyst deactivation due to the presence of As(V) is likely to be caused by adsorbed As(V) blocking the solid-solution interface.^[40,41] We therefore also constructed a rate law where only adsorbed As(V) decreases the reaction rate. The concentration of adsorbed As(V) was estimated using a surface complexation model (SCM) developed in our previous work.^[45] This model predicts adsorption as a function of pH and ionic strength, and crucially incorporates competitive adsorption, for example As(V) versus As(III). We considered the simple case that the reaction rate decreases linearly with the increasing concentration of adsorbed As(V), arriving at Equation S17. This rate equation is named the “SCM-constrained As(V) model”.

The results of this model are presented in Figure 8. Firstly, the PFO shape of the data at later times is reproduced using this model (Figure 8a). It is only at the end of each reaction that PFO linearization fails (Figure 8b). This is because once the concentration of adsorbed As(V) reaches $\frac{1}{j}$, the rate falls to zero and the reaction ceases. Secondly, when the initial concentration of As(III) $\geq 3.5 \text{ mg L}^{-1}$, the initial rate is independent of

the As(III) concentration (Figure 8c), providing the zero-order kinetics identified by initial rates analysis. Within this concentration range, the sensitivity parameter, j , is also constant ($0.131 \pm 0.009 \text{ mg}^{-1}$, with the reaction ceasing once the concentration of adsorbed As(V) reaches $7.6 \pm 0.5 \text{ mg g}^{-1}$). The sensitivity of meso-TiO₂ to deactivation by As(V) adsorption is therefore independent of the concentration of As(III). This model fails when the initial concentration of As(III) is $< 3.5 \text{ mg L}^{-1}$, since the rate constant k^\ddagger increases with decreasing As(III) concentrations. Importantly, this As(V) deactivation model provides a rate constant that is significantly less dependent upon the initial concentration of As(III) than the PFO rate constant k_1 (Figure 8d). The success of this preliminary model to reconcile initial rates and data at later times indicates that the disguised zero-order kinetics of meso-TiO₂ are caused by As(V) deactivation of the catalyst.

Since initial rates are independent of the concentration of As(III) (Figure 6c) and the addition of phosphate enhances reaction rates (Supporting Information section 6), we suggest that the deactivation of meso-TiO₂ due to adsorbed As(V) is caused by As(V) interfering with the generation of ROS

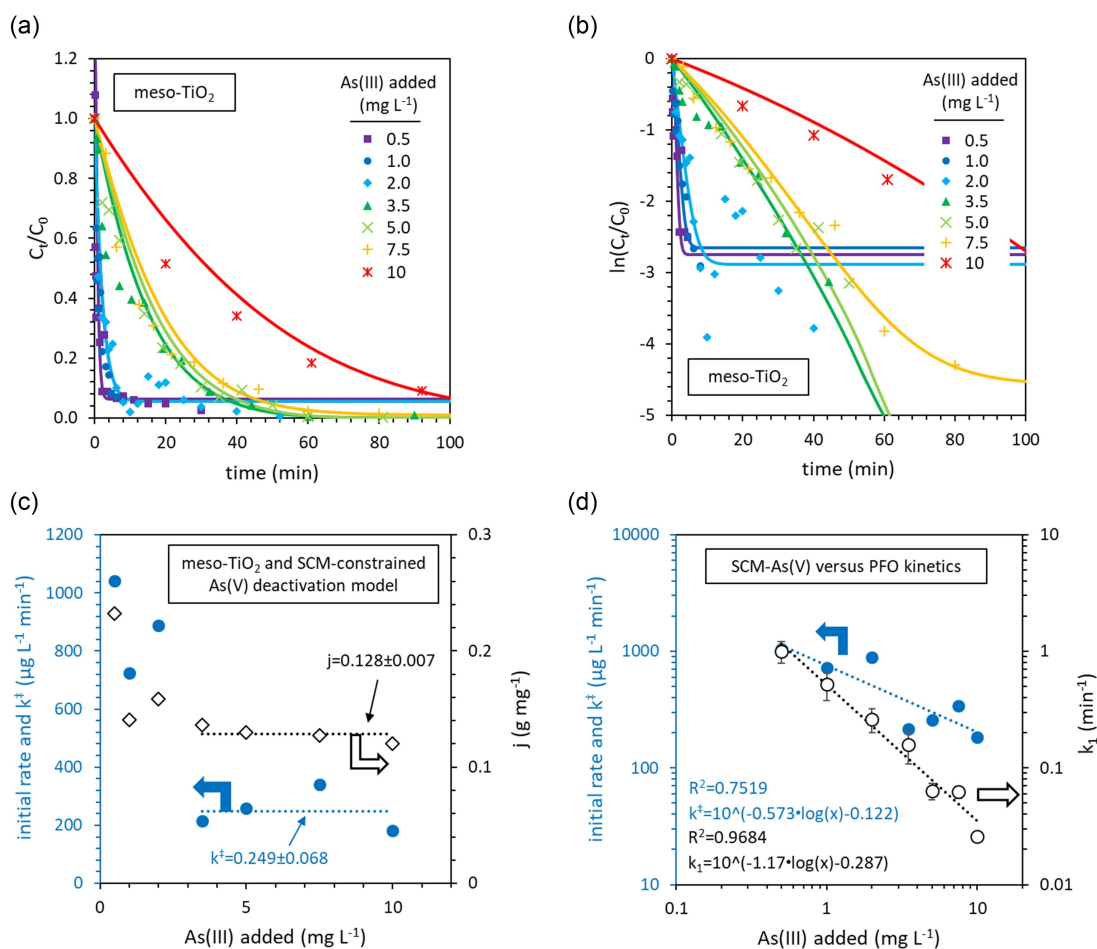


Figure 8. SCM-constrained As(V) deactivation kinetics for the photocatalytic oxidation of As(III) in the presence of meso-TiO₂. (a, b) Comparison of the fitted model and experimental data. (c) The influence of the As(III) concentration on the initial rate, the rate constant k^\ddagger , and the sensitivity factor j . (d) Values of k^\ddagger calculated from experimental data are less influenced by [As(III)] than the PFO rate constant k_1 .

intermediates, rather than by As(V) blocking the access of As(III) to the catalyst surface.

First-order kinetics of meso-TiO₂/Fe₂O₃ explained by the late stage partitioning of As(III) to the adsorbed phase

Langmuir-Hinshelwood (LH) kinetics are often used to describe adsorption-controlled catalysis,^[68] however, to our knowledge, only a couple of papers have considered LH kinetics for the photocatalytic oxidation of As(III).^[51,52] The LH rate equation is first-order with respect to the concentration of adsorbed As(III), as calculated using the Langmuir adsorption isotherm model.^[68] LH kinetics successfully introduced some of the curvature in $\ln(C_t/C_0)$ observed for meso-TiO₂/Fe₂O₃ when the initial concentration of As(III) ≥ 3.5 mg L⁻¹ (Supporting Information Figure S17). However, we encounter two problems: (1) the initial rates do not conform to linearized LH kinetics, and (2) the rate constant (k_{LH}) decreases exponentially with increasing initial As(III) concentrations. The Langmuir-Hinshelwood kinetic model notably does not consider interference by competitor ions,^[68] such as the As(V) that appears to deactivate meso-TiO₂.

We subsequently used surface complexation modelling (SCM) to investigate how the concentration of adsorbed As(III) changes as the photooxidation reaction progresses, using discrete TiO₂ and Fe₂O₃ surface phases and including the competitive adsorption of As(V). This model predicts a significant increase in the partitioning of As(III) to the adsorbed phase as the final 20% of As(III) is oxidized (Figure 9a). This coincides with the increased steepness in the linearized PFO plots of experimental data at $\ln(C_t/C_0) \approx -1.5$ (Figure 7c), suggesting that the experimental oxidation kinetics are explained by the partitioning of As(III) between aqueous and adsorbed phases.

We therefore modified the Langmuir-Hinshelwood kinetic model so that the concentration of adsorbed As(III) is calculated using the SCM, thereby incorporating the competitive adsorption of As(V) (Eq. S18 and Figure 9b). Our new SCM-constrained model best captures the observed curvature in plots of $\ln(C_t/C_0)$ versus time (Figure 9c). Langmuir-Hinshelwood kinetics provide only some of the observed curvature, since whilst the Langmuir adsorption isotherm predicts increased partitioning of As(III) to the surface as oxidation progresses, there is no sharp feature after 78% of As(III) has been oxidized (Supporting Information Figure S18). The SCM-constrained model also greatly reduces

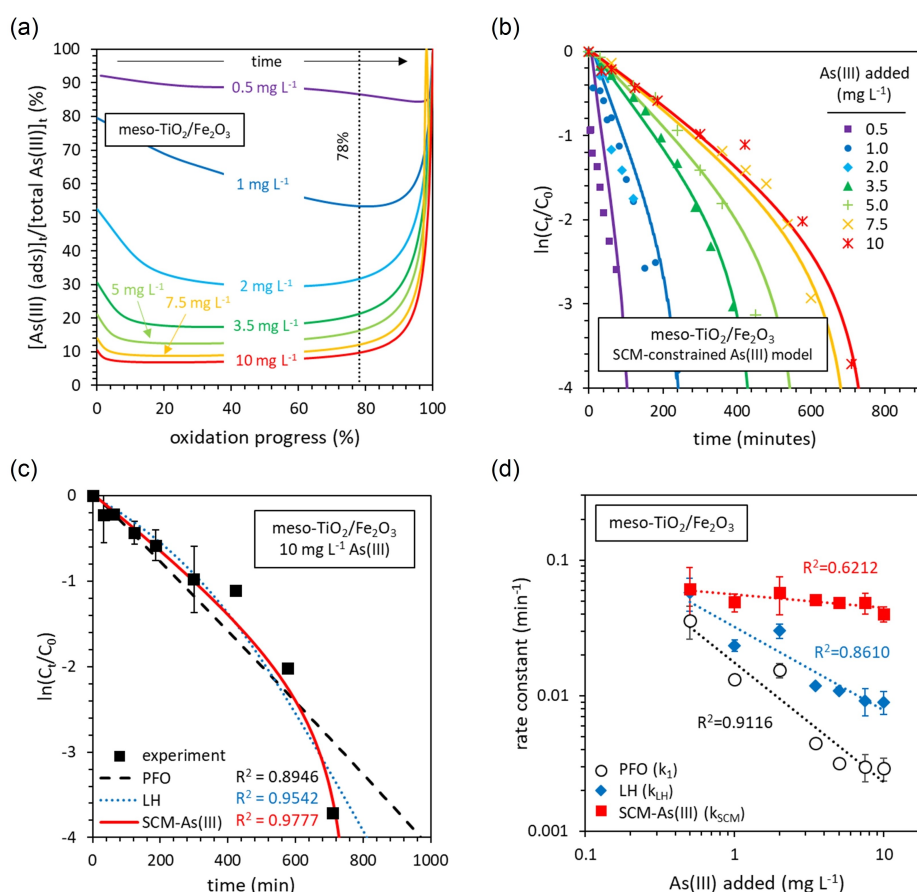


Figure 9. Explaining the kinetics of As(III) photocatalytic oxidation in the presence of meso-TiO₂/Fe₂O₃ using the SCM-constrained As(III) kinetic model. (a) The SCM-predicted partitioning of As(III) between adsorbed and aqueous phases, with different total arsenic concentrations, as photocatalytic oxidation progresses. The 78% line is equivalent to $\ln(C_t/C_0) \approx -1.5$. The catalyst concentration was 0.1 g L⁻¹, and the SCM methodology is presented in the Supporting Information. (b) The SCM-constrained As(III) kinetic model fitted to data at later times in the form $\ln(C_t/C_0)$. (c) A comparison of models fitted to data at later times in the form $\ln(C_t/C_0)$. (d) The influence of As(III) concentration on the rate constants calculated for each model.

the conditionality of the rate constant towards the initial As(III) concentration, compared with the PFO and LH kinetic models (Figure 9d). These results indicate that the photocatalytic oxidation kinetics of meso-TiO₂/Fe₂O₃ are controlled by the adsorption of As(III), competing with As(V) for surface sites.

A comparison of different mechanisms of As(III) oxidation

A valid rate equation will yield a rate constant that is independent of the initial As(III) concentration, i.e [Eq. (1)],

$$\frac{\Delta \log(k)}{\Delta \log([\text{As(III)}]_{\text{added}})} = 0 \quad (1)$$

For meso-TiO₂, the As(V) deactivation model recreates the experimentally observed disguised zero-order kinetics and yields the most consistent rate constants (Figure 10). Consistent rate constants cannot be obtained for meso-TiO₂ using (a) PFO kinetics or (b) As(III) adsorption-controlled kinetics (e.g. LH kinetics). This mechanism is consistent with phosphate experiments, which suggest that the oxidation of As(III) proceeds via ROS intermediates (Supporting Information Figure S14), and that it is the generation of these ROS intermediates that determines the reaction rate.

In contrast, the most consistent rate constants for meso-TiO₂/Fe₂O₃ are achieved using the SCM-constrained As(III) and As(V) adsorption models (Figure 10). Of these, only the SCM-constrained As(III) adsorption rate equation gives the first-order relationship between the concentration of adsorbed As(III) and initial rates that is observed experimentally (Figure 6d).

Despite possessing a greater adsorption capacity (and significant parasitic absorption, presumably decreasing the rate of ROS generation), the kinetics of meso-TiO₂/Fe₂O₃ depend on

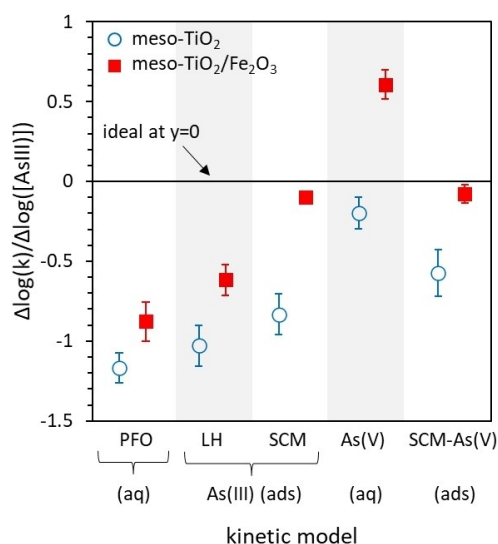


Figure 10. Rate constant dependence upon initial As(III) concentrations, for each kinetic model investigated in this work. Accurate rate equations will provide a rate constant that is independent of [As(III)], and thus the closer to zero that $\frac{\Delta \log(k)}{\Delta \log([\text{As(III)}]_{\text{added}})}$ is, the more valid the kinetic model is.

[As(III) (ads)], whilst the kinetics of meso-TiO₂ do not. To explain this, we consider the speciation of arsenic adsorbed onto the TiO₂ and Fe₂O₃ surfaces of the composite photocatalyst. The SCM achieves the best fit to experimental data when covalently bonded, inner-sphere (>SO)₂AsOH is the major surface complex for Fe₂O₃-sorbed As(III) at pH 7^[45] (where >S denotes the metal oxide surface). In contrast, meso-TiO₂ is best fit using a mix of inner-sphere (>SO)₂AsO⁻ and the weakly bound outer-sphere (hydrogen-bonded) >SOH₂⁺-AsO(OH)₂⁻ surface complex. Equilibrium constants for these reactions are greater for Fe₂O₃ (logK=5.3) than for meso-TiO₂ (logK=3.0 and 4.0 respectively). The As(III) surface complexes formed on the TiO₂ surface are therefore weaker than those formed on the Fe₂O₃ surface, and TiO₂-sorbed As(III) is therefore more rapidly substituted for As(V) than Fe₂O₃-sorbed As(III).

Consequently, whilst meso-TiO₂ shows an approximately linear decrease in the concentration of TiO₂-sorbed As(III) with increasing reaction progress, As(III) adsorbed on the minority TiO₂ surface phase of meso-TiO₂/Fe₂O₃ is rapidly replaced by As(V) (Figure 11). The model predicts that after 10% of all As(III) has been oxidized, the concentration of TiO₂-sorbed As(III) is twenty times less in the meso-TiO₂/Fe₂O₃ system than the meso-TiO₂ system (with an initial As(III) concentration of 10 mg L⁻¹). After 20% of all As(III) has been oxidized, this difference increases to a factor of 40. Consequently, whilst the kinetics of single-component meso-TiO₂ depend principally upon the generation of ROS, the availability of adsorbed As(III) becomes a rate limiting factor for the meso-TiO₂/Fe₂O₃ system (Figure 11).

Despite the SCM predicting that the As(III) adsorbed on the TiO₂ surface is rapidly substituted for As(V), meso-TiO₂/Fe₂O₃ does not show signs of As(V) deactivation: the reaction proceeds to completion in Figure 5b, and the initial rates are best described by the As(III) adsorption model rather than the As(V) deactivation model. Whilst the SCM predicts that the Fe₂O₃ sorbent phase does not prevent TiO₂ from becoming

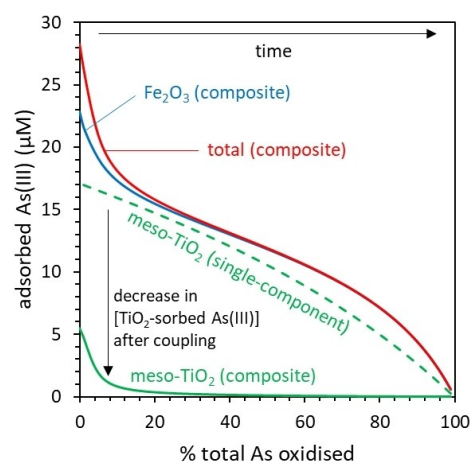


Figure 11. Changes in the concentration of adsorbed As(III) with progressive oxidation, predicted using a component additive surface complexation model (CA-SCM). The conditions are 10 mg L⁻¹ initial As(III), 0.1 g L⁻¹ photocatalyst, 0.01 M NaCl, pH 7.

saturated with As(V), the sorbent phase may prevent catalyst fouling by maintaining a high concentration of adsorbed As(III) at the overall composite surface. For instance, in the meso-TiO₂/Fe₂O₃ system, there is 23 times more As(III) adsorbed on Fe₂O₃ versus TiO₂ after 10% oxidation, increasing to a factor of 43 after 20% oxidation (Figure 11). The surface diffusion of ROS intermediates has been reported (with distances of up to tens of microns)^[69] raising the possibility that ROS generated by the TiO₂ phase migrates to oxidize the more prevalent Fe₂O₃-sorbed As(III).

Concept for the photocatalytic oxidation of As(III) using meso-TiO₂/Fe₂O₃

Figure 12 shows a schematic model illustrating the photocatalytic oxidation of As(III) by meso-TiO₂/Fe₂O₃. Firstly, the majority of incident photons (88% at 368 nm) are parasitically absorbed by the Fe₂O₃ component with insignificant oxidation of As(III).^[18] Secondly, despite being thermodynamically favourable, charge transfer from meso-TiO₂ to Fe₂O₃ is insignificant, with the TiO₂-Fe₂O₃ heterojunction prepared under this synthesis method failing to enhance photocatalysis. Thirdly, the adsorption of As(V) deactivates the photocatalyst, principally by preventing the generation of reactive oxygen species (ROS) intermediates. Finally, due to the low availability of As(III) adsorbed on the TiO₂ surface, ROS potentially migrates to the Fe₂O₃ phase before inducing the oxidation of Fe₂O₃-sorbed As(III). In this model, it appears that incorporation of the Fe₂O₃ sorbent phase does not prevent photocatalyst deactivation by suppressing the adsorption of As(V) onto the TiO₂ surface,^[66] but rather by maintaining a local concentration of As(III) on the neighbouring Fe₂O₃ surface.

The relative importance of these mechanisms can be evaluated semi-quantitatively. When light power $\leq 2.5 \text{ mW cm}^{-2}$

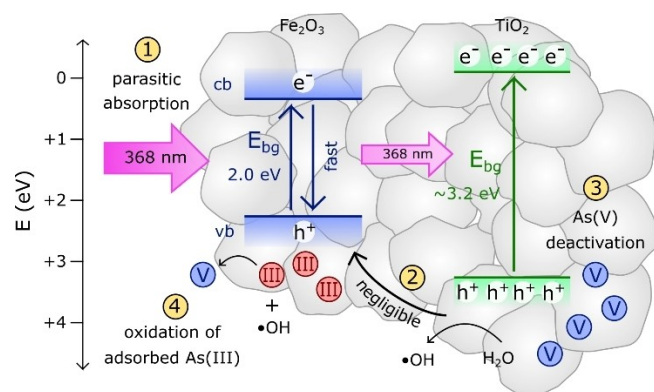


Figure 12. Concept schematic illustrating the photocatalytic oxidation of As(III) by meso-TiO₂/Fe₂O₃. (1) The majority of incident photons (88% at 368 nm) are parasitically absorbed by the Fe₂O₃ component. (2) Despite being thermodynamically favourable, the transfer of positive holes from the valence band of meso-TiO₂ to Fe₂O₃ is insignificant. (3) The adsorption of As(V) deactivates the photocatalyst. (4) Reactive oxygen species (ROS) such as the hydroxyl radical oxidize adsorbed As(III), the majority of which is found adsorbed to the Fe₂O₃ surface. As(III) is represented by red circles and As(V) by blue circles.

the difference in reaction rates is greatest (~60 times) whilst the TiO₂ electron-hole recombination rates in meso-TiO₂ and meso-TiO₂/Fe₂O₃ are equivalent. Firstly, the component-additive TAS model developed in this work indicates that the TiO₂-Fe₂O₃ heterojunction provides zero increase to the rate of As(III) oxidation. In contrast, UV-Vis absorption spectroscopy indicates that parasitic light absorption accounts for 88% of the observed difference in reaction rates. After considering parasitic light absorption, a 7.5 ± 1.4 factor difference in oxidation rates remains unexplained. Photocatalytic activity is often linked to surface area^[70] and we previously identified that only $32 \pm 1\%$ of the exposed meso-TiO₂/Fe₂O₃ surface is meso-TiO₂.^[45] Assuming a linear relationship between surface area and photocatalytic activity, the iron oxide surface coating would account for up to 68% of the difference in reaction rates. After considering possible surface area effects, a 2.4 ± 0.5 factor difference in rates remains unaccounted for and is therefore attributed to the different reaction mechanisms, where the availability of adsorbed As(III) becomes a limiting factor once meso-TiO₂ is coupled with Fe₂O₃ (as indicated by our application of surface complexation modelling). Consequently, parasitic absorption is likely the principle mechanism determining photocatalytic oxidation rates in the TiO₂/Fe₂O₃ composites, with the change in rate law acting as a secondary influence.

Conclusion

This study investigated, for the first time, the mechanisms by which coupling a TiO₂ photocatalyst with an iron oxide sorbent phase influences reaction kinetics in the photocatalytic oxidation of As(III). Our key finding is that oxidation kinetics are decreased after sorbent-coupling, primarily due to parasitic light absorption by the Fe₂O₃ sorbent phase, and secondarily due to changes in the rate law, from being limited by the generation of ROS intermediates (disguised zero-order kinetics) to being limited by the availability of adsorbed As(III) (first-order kinetics). Moreover, our TAS studies show that the TiO₂-Fe₂O₃ heterojunction formed by this synthesis method does not effectively separate charge carriers.

To evaluate how material coupling influences As(III) oxidation kinetics, we developed new hybrid experimental-modelling approaches and our key innovations are: (i) The quantification of parasitic absorption using UV-Vis spectroscopy and component additivity; (ii) Evaluation of the role of the heterojunction using a combination of transient absorption spectroscopy (TAS) and component additivity; (iii) The first application of a multi-sorbate surface complexation model (SCM) to constrain competitive adsorption-controlled kinetics more accurately than the single-sorbate Langmuir-Hinshelwood model; and (iv) The first application of a As(V)-deactivation kinetic model to explain disguised zero-order kinetics in the photocatalytic oxidation of As(III). These approaches should help understand the influence of mineral coupling in other composite photocatalyst systems, and the SCM-constrained kinetic model should be used in place of Langmuir-Hinshelwood kinetics when modelling As(III) oxidation due to the competitive adsorption of As(V).

Current sorbent media (e.g. iron oxides) could be readily substituted with meso-TiO₂/Fe₂O₃, maintaining high arsenic removal capacities whilst imparting modest photocatalytic capabilities. This may be advantageous for single-step, single-reactor treatments, simplifying construction and maintenance of treatment plants^[46] given that maintenance is a major reason for the failure of current treatment plants.^[15] However, when it is necessary to improve oxidation kinetics (and thus energy efficiency), it will be important to reduce the parasitic light absorption of the sorbent phase, for example replacing Fe₂O₃ with a wide bandgap sorbent such as aluminum oxide (Al₂O₃, 6 eV)^[71] which is already used as an arsenic sorbent.^[15] Potentially, TiO₂ (bandgap 3.0–3.2 eV) can be substituted for photocatalysts such as graphitic carbon nitride (g-C₃N₄, 2.7 eV) which not only absorbs visible light, but is also a poor arsenic sorbent and therefore should not suffer from the same As(V) deactivation as TiO₂.^[51,72] In the case of titania-iron oxide composites, alternative synthesis routes and composite architectures (e.g. Janus particles) should be investigated to achieve charge carrier separation across the heterojunction.^[73] Whilst efficient removal of As(V) using meso-TiO₂/Fe₂O₃ after 9 regeneration cycles has been demonstrated previously,^[28] future engineering studies should also investigate potential changes to photocatalytic oxidation kinetics after regeneration of the photocatalyst, and correlate any changes in the kinetics to material properties (e.g. surface characterization using SEM and XPS).^[74,75]

Experimental Section

Materials and reagents

All chemicals were reagent or analytical grade (as detailed in Supporting Information Table S1). Stock solutions of As(III) and As(V) (1000 mg L⁻¹) were prepared from As₂O₃ and Na₂HAsO₄·7H₂O respectively and stored in opaque plastic bottles, refrigerated at 3 °C to prevent changes in the speciation. Solutions of 10 mM HEPES were prepared from HEPES free acid (powder). Groundwater was collected from an arsenic-contaminated area of West Bengal, India as described in our previous work^[76] and characterized in Supporting Information section 1.2.

Synthesis of materials

Meso-TiO₂ and meso-TiO₂/Fe₂O₃ were synthesized following the procedure of Zhou et al.^[28] as per our previous work.^[45,46] First, meso-TiO₂ was prepared via a sol-gel procedure using P123 as a structure-directing agent: a solution of ethanolic P123 (1 g in 12 mL) was added dropwise to Ti(IV) n-butoxide in concentrated HCl (2.7 g in 3.2 g). After stirring to evaporate the solvent under ambient conditions, the sol-gel product was calcined at 350 °C for four hours and crushed. Secondly, meso-TiO₂ was coupled with Fe₂O₃, aiming to give a 1:1 mass ratio of TiO₂ to Fe₂O₃: meso-TiO₂ (1.5 g) was added to a solution of 0.60 M ethanolic iron nitrate (30 mL) and after evaporating the solvent at 50 °C with stirring, the product was calcined at 300 °C for six hours and crushed. A Fe₂O₃ reference sample was prepared similarly, albeit without addition of meso-TiO₂.

Materials characterisation

The crystal phases of meso-TiO₂/Fe₂O₃ and the reference samples were identified by X-ray diffraction (XRD) using a PANalytical MPD. Crystallite diameters were estimated from the peak broadening using the Scherrer equation (Supporting Information equation S1). The BET-specific surface area and pore size were determined using Brunauer-Emmett-Teller (BET) and Barrett-Joyner-Halenda (BJH) analysis respectively, from N₂ adsorption-desorption isotherms measured using a Quantachrome Autosorb iQ. All samples were outgassed at 200 °C for 20 h prior to analysis. The elemental composition was determined by X-ray fluorescence (XRF) using a PANalytical Epsilon 3 XLE, and the mass ratio between meso-TiO₂ and Fe₂O₃ components was calculated as described in Supporting Information section 2.4.

Component additive analysis of UV-Vis absorbance

UV-Vis spectra were recorded using a Shimadzu UV-2700 spectrophotometer, equipped with an integrating sphere, and analysed using the Beer-Lambert law and the Kubelka-Munk function as described in Supporting Information section 1.5.

To quantify the extent of parasitic absorption, a component additive prediction of absorbance (*A*) was calculated for the meso-TiO₂/Fe₂O₃ composite photocatalyst, using a linear combination of the data collected for meso-TiO₂ and Fe₂O₃ reference samples, weighted according to the mass fraction of each component:

$$A_{\text{comp}} = m_a A_b + m_b A_a \quad (2)$$

where *comp* denotes the composite photocatalyst, *a* and *b* denote the reference samples (i.e. meso-TiO₂ and Fe₂O₃), *A_{comp}* is the predicted absorbance of the composite photocatalyst, *m_i* is the mass fraction of component *i* within the composite photocatalyst (calculated using XRF), and *A_i* is the experimentally determined absorbance of the single-component reference sample *i*.^[77]

The extinction coefficient of the composite photocatalyst, ϵ_{comp} , was calculated similarly:

$$\epsilon_{\text{comp}} = m_a \epsilon_a + m_b \epsilon_b \quad (3)$$

where ϵ_i is the experimentally calculated extinction coefficient of the single-component reference sample *i* (L g⁻¹ cm⁻¹).

The proportion of incident photons absorbed by each component (meso-TiO₂ or Fe₂O₃) within the composite was then estimated using the equation:

$$\theta_i = \frac{m_i A_i}{A_{\text{comp}}} \quad (4)$$

where θ_i represents the fraction of the total photons (at the given wavelength) absorbed by the composite photocatalyst that are absorbed by component *i*, and *A_i* is the absorbance (or extinction coefficient) of component *i*.

Transient absorption spectroscopy (TAS)

TAS spectra were recorded as described in Supporting Information section 1.6. Treating meso-TiO₂ and Fe₂O₃ phases within the composite photocatalyst as non-interacting components, a component additive prediction was calculated to assess the possibility of charge transfer across the TiO₂-Fe₂O₃ heterojunction. First, to

determine transient absorption half-lives more accurately, transient absorption decay curves were modelled using a power-law decay function with the equation:

$$[h^+]_t = At^{-\alpha} \quad (5)$$

where $[h^+]_t$ is the concentration of holes at time t (represented by the change in optical density, ΔOD), t is time (seconds), and A and α are fitting parameters.^[78] Parameters A and α were optimized to improve the goodness of fit (R^2) between modelled and experimental data. Data before 0.1 and after 100 ms were excluded from data fitting, due to interference from the laser pulse and loss of material suspension respectively.

TAS spectra were normalized to unity at $t=100 \mu\text{s}$, with the normalized value of A calculated via the rearrangement of Equation (5), giving:

$$A_{\text{normalised}} = \frac{1}{0.0001^{-\alpha}} \quad (6)$$

Transient absorption half-lives ($t_{1/2}$) were then calculated using rearrangement of Equation (5) to give:

$$t_{1/2} = \left(\frac{1}{2} \cdot \frac{1}{A_{\text{normalised}}} \right)^{-\frac{1}{\alpha}} \quad (7)$$

The component additive prediction of meso-TiO₂/Fe₂O₃ transient absorption decay was calculated using a linear combination of meso-TiO₂ and Fe₂O₃ power law decay functions. First, the distribution of the absorbed laser pulse at $\lambda=355 \text{ nm}$ between meso-TiO₂ and Fe₂O₃ components was estimated as the product of each component's optical density at $\lambda=355 \text{ nm}$ and its mass fraction (Equation (4)), incorporating Equations S7 and S19). The component additive prediction of transient absorption decay was then calculated using the formula:

$$\Delta OD(t, \lambda)_{\text{comp}} = \theta(0, 355 \text{ nm})_a \Delta OD(t, \lambda)_a + \theta(0, 355 \text{ nm})_b \Delta OD(t, \lambda)_b \quad (8)$$

where $\Delta OD(t, \lambda)_{\text{comp}}$ is the change in optical density (i.e. the transient absorption) of the composite photocatalyst at time t and wavelength λ , $\theta(0, 355 \text{ nm})_i$ is the proportion of the laser pulse absorbed by component i (Equation (4)), and $\Delta OD(t, \lambda)_i$ is the experimentally observed transient absorption of component i at time t and wavelength λ .

Photocatalytic oxidation kinetics

The photocatalytic oxidation of As(III) was measured in a 100 mL beaker with a diameter of 5.4 cm placed on top of a magnetic stirrer, illuminated overhead using a horizontal ultraviolet lamp ($\lambda=368 \text{ nm}$, 18 mW). The light intensity across the sample surface area was measured using a power meter (PM100, Thorlabs) connected to a power sensor (S120UV, Thorlabs). The photoreactor was housed within an opaque black plastic box and a UV-transparent fused-silica lid was used to prevent evaporation. To vary the light power, the distance between the lamp and the sample was varied between 2.5 and 31 cm (0.7–14 mW cm⁻²). A diagram of this set-up is presented in Supporting Information Figure S1.

Powders were suspended (0.1 g L⁻¹) in 100 mL media (10 mM HEPES, with or without addition of 10 mg L⁻¹ phosphate) and spiked with As(III) (0.5–10 mg L⁻¹). Suspensions were adjusted to

pH 7.3 ± 0.1 through the addition of small volumes of 0.01 or 1 M HCl and NaOH, since the As(III) contaminated waters in South Asia are typically between pH 7 and 8.^[33–35] Suspensions were magnetically stirred overnight in the dark to achieve equilibrium adsorption. The UV lamp was warmed up for ten minutes before the sample was irradiated. The time at which the suspension was first irradiated was designated $t=0$. At regular time intervals, 1 mL aliquots were extracted from the suspension and filtered using a 0.45 μm nylon membrane to remove solids. Samples were kept in the dark prior to analysis to prevent further photooxidation.

Concentrations of As(III) and total As were determined using anodic stripping voltammetry (ASV) and a method based upon established procedures,^[76,79,80] described in detail in Supporting Information section 1.8. Oxidation progress was monitored using [As(III) (aq)] rather than [As(V) (aq)] as this is expected to give a more accurate measure of oxidation kinetics, especially at low total arsenic concentrations.^[81] The average uncertainty in the measurement was 10%.

Kinetic modelling

The kinetics of As(III) oxidation in the presence of meso-TiO₂ and meso-TiO₂/Fe₂O₃ were investigated using two methods for corroboration: the method of initial rates and analysis of data at later times.^[82] Initial rates were calculated by fitting a linear regression to the initial linear region observed when [As(III) (aq)] is plotted as a function of time. Data at later times was analysed using pseudo-first order (PFO) kinetics, Langmuir-Hinshelwood (LH) kinetics, a new As(V) deactivation model, and a new As(III) adsorption-constrained kinetic model, which uses the surface complexation model (SCM) developed in a previous work.^[45] Full details of the modelling are presented in Supporting Information section 1.10.

Total arsenic removal

Total arsenic removal experiments were prepared as per the kinetic experiments (0.1 g L⁻¹ photocatalyst, pH 7.3 ± 0.1, 100 mL volume), however only 1 mg L⁻¹ As(III) was added. The background media was either 10 mM HEPES, 10 mM HEPES spiked with 50 mg L⁻¹ PO₄³⁻, or a natural groundwater sampled from an arsenic contaminated region of West Bengal. After stirring in the dark overnight to achieve equilibrium adsorption, the *pre-oxidation* sample was collected. After photooxidation using ultraviolet light was complete, the *post-oxidation* sample was collected (after a minimum of 30 minutes irradiation for meso-TiO₂ and a minimum of 120 minutes for meso-TiO₂/Fe₂O₃, after which < 20 $\mu\text{g L}^{-1}$ As(III) (aq) remained). The concentration of total As was determined using ASV, and total arsenic removal was calculated by subtracting the concentration of aqueous arsenic remaining from the concentration of arsenic initially added.

Acknowledgements

This work was supported by the Engineering and Physical Sciences Research Council (EPSRC) [grant number EP/N509486/1] and the EPSRC Centre for Doctoral Training in the Advanced Characterisation of Materials (CDT ACM) [grant number EP/L015277/1]. A.K. thanks Imperial College for a Junior Research Fellowship, the EPSRC for a Capital Award Emphasising Support for Early Career Researchers, and the Royal Society for an Equipment Grant (RSGVR1\180434).

Conflict of Interest

The authors declare no conflict of interest.

Data Availability Statement

The data that support the findings of this study are openly available in Zenodo at 10.5281/zenodo.3975646, reference number 3975646.

Keywords: arsenic · composite · photocatalysis · photocatalytic oxidation · water treatment

- [1] S. Flanagan, R. Johnston, Y. Zheng, *Bull. W. H. O.* **2012**, *90*, 839–846.
- [2] R. N. Ratnaik, *Postgrad. Med. J.* **2003**, *79*, 391–396.
- [3] M. Shahid, N. K. Niazi, C. Dumat, R. Naidu, S. Khalid, M. M. Rahman, I. Bibi, *Environ. Pollut.* **2018**, *242*, 307–319.
- [4] N. R. Nicomel, K. Leus, K. Follens, P. Van Der Voort, G. Du Laing, *Int. J. Environ. Res. Public Health* **2015**, *13*, 1–24.
- [5] W. Wong, H. Y. Wong, A. B. M. Badruzzaman, H. H. Goh, M. Zaman, *Nanotechnology* **2017**, *28*, 042001.
- [6] P. L. Smedley, in *Arsen. Groundw. a World Probl.* (Ed.: T. Appelo), International Association Of Hydrogeologists Publication, **2008**, pp. 1–34.
- [7] R. B. Johnston, S. Hanchett, M. H. Khan, *Nat. Geosci.* **2010**, *3*, 2–3.
- [8] M. Shafiquzzaman, M. S. Azam, I. Moshima, J. Nakajima, *J. Heal. Popul. Nutr.* **2009**, *27*, 674–683.
- [9] M. F. Ahmed, in *Proc. BUET-UNU Int. Work. Technol. Arsen. Remov. from Drink. Water, Dhaka*, Bangladesh University Of Engineering And Technology, **2001**, pp. 251–269.
- [10] H. Yang, W.-Y. Lin, K. Rajeshwar, *J. Photochem. Photobiol. A* **1999**, *123*, 137–143.
- [11] J. Gamage, Z. Zhang, *Int. J. Photoenergy* **2010**, *2010*, 764870.
- [12] A. Ibbadon, P. Fitzpatrick, *Catalysts* **2013**, *3*, 189–218.
- [13] D. Gerrity, B. Mayer, H. Ryu, J. Crittenden, M. Abbaszadegan, *Water Res.* **2009**, *43*, 1597–1610.
- [14] N. Yahya, F. Aziz, N. A. Jamaludin, M. A. Mutalib, A. F. Ismail, W. N. W. Salleh, J. Jaafar, N. Yusof, N. A. Ludin, *J. Environ. Chem. Eng.* **2018**, *6*, 7411–7425.
- [15] A. Kumar, M. B. Roy, P. K. Roy, J. M. Wallace, *J. Inst. Eng. Ser. A* **2019**, *100*, 253–259.
- [16] L. N. Pincus, A. W. Lounsbury, J. B. Zimmerman, *Acc. Chem. Res.* **2019**, *52*, 1206–1214.
- [17] L. N. Pincus, F. Melnikov, J. S. Yamani, J. B. Zimmerman, *J. Hazard. Mater.* **2018**, *358*, 145–154.
- [18] S. Sun, C. Ji, L. Wu, S. Chi, R. Qu, Y. Li, Y. Lu, C. Sun, Z. Xue, *Mater. Chem. Phys.* **2017**, *194*, 1–8.
- [19] F. S. Zhang, H. Itoh, *Chemosphere* **2006**, *65*, 125–131.
- [20] M. D'Arcy, D. Weiss, M. Bluck, R. Vilar, *J. Colloid Interface Sci.* **2011**, *364*, 205–212.
- [21] L. Yu, X. Peng, F. Ni, J. Li, D. Wang, Z. Luan, *J. Hazard. Mater.* **2013**, *246–247*, 10–17.
- [22] H. Su, X. Lv, Z. Zhang, J. Yu, T. Wang, *J. Porous Mater.* **2017**, *24*, 1227–1235.
- [23] F. Beduk, *Environ. Technol. (United Kingdom)* **2016**, *37*, 1790–1801.
- [24] M. Deng, X. Wu, A. Zhu, Q. Zhang, Q. Liu, *J. Environ. Manage.* **2019**, *237*, 63–74.
- [25] Y. Wang, P. Zhang, T. C. Zhang, G. Xiang, X. Wang, S. Pehkonen, S. Yuan, *Nanoscale Adv.* **2020**, *2*, 2018–2024.
- [26] Y. Wang, Y. Zhang, T. C. Zhang, G. Xiang, X. Wang, S. Yuan, *ACS Appl. Mater. Interfaces* **2020**, *3*, 8495–8504.
- [27] X. Liu, Y. Wang, T. C. Zhang, G. Xiang, X. Wang, S. Yuan, *Ind. Eng. Chem. Res.* **2021**, *60*, 528–540.
- [28] W. Zhou, H. Fu, K. Pan, C. Tian, Y. Qu, P. Lu, C. Sun, *J. Phys. Chem.* **2008**, *112*, 19584–19589.
- [29] J. Schmidt, W. Vogelsberger, *J. Phys. Chem. B* **2006**, *110*, 3955–3963.
- [30] N. Xu, Y. Gao, *Appl. Geochem.* **2008**, *23*, 783–793.
- [31] C. Siffert, B. Sulzberger, *Langmuir* **1991**, *7*, 1627–1634.
- [32] J. G. Wiederhold, S. M. Kraemer, N. Teutsch, P. M. Borer, A. N. Halliday, R. Kretzschmar, *Environ. Sci. Technol.* **2006**, *40*, 3787–3793.
- [33] J. M. McArthur, D. M. Banerjee, K. A. Hudson-Edwards, R. Mishra, R. Purohit, P. Ravenscroft, A. Cronin, R. J. Howarth, A. Chatterjee, T. Talukder, D. Lowry, S. Houghton, D. K. Chadha, *Appl. Geochem.* **2004**, *19*, 1255–1293.
- [34] S. J. Hug, O. X. Leupin, M. Berg, *Environ. Sci. Technol.* **2008**, *42*, 6318–6323.
- [35] J. C. Ayers, S. Goodbred, G. George, D. Fry, L. Benneyworth, G. Hornberger, K. Roy, M. R. Karim, F. Akter, *Geochem. Trans.* **2016**, *17*, 4.
- [36] J. G. Hering, I. A. Katsoyiannis, G. A. Theoduloz, M. Berg, S. J. Hug, *J. Environ. Eng. (United States)* **2017**, *143*, 1–9.
- [37] S. R. Pendlebury, X. Wang, F. Le Formal, M. Cornuz, A. Kafizas, S. D. Tilley, M. Grätzel, J. R. Durrant, *J. Am. Chem. Soc.* **2014**, *136*, 9854–9857.
- [38] S. J. A. Moniz, S. A. Shevlin, X. An, Z. X. Guo, J. Tang, *Chem. A Eur. J.* **2014**, *20*, 15571–15579.
- [39] A. Jiamprasertboon, A. Kafizas, M. Sachs, M. Ling, A. M. Alotaibi, Y. Lu, T. Siritanon, I. P. Parkin, C. J. Carmalt, *Chem. A Eur. J.* **2019**, *25*, 11337–11345.
- [40] A. Katz, A. Mcdonagh, L. Tijing, H. K. Shon, *Crit. Rev. Environ. Sci. Technol.* **2015**, *45*, 1880–1915.
- [41] V. Vaiano, G. Iervolino, D. Sannino, L. Rizzo, G. Sarno, A. Farina, *Appl. Catal. B* **2014**, *160–161*, 247–253.
- [42] Y. Li, N. Zhang, J. Chen, R. Li, L. Li, K. Li, *J. Nanopart. Res.* **2016**, *18*, 1–8.
- [43] W. Fu, D. L. Lu, H. Yao, S. Yuan, W. Wang, M. Gong, Z. H. Hu, *Environ. Sci. Pollut. Res. Int.* **2020**, *27*, 18434–18442.
- [44] C. Mohan, R. Vinodh, B. Sundaravel, A. Abidov, M. Mei, W. Seog, H. Jang, *J. Inst. Chem.* **2016**, *62*, 199–208.
- [45] J. C. Bullen, J. P. L. Kenney, S. Fearn, A. Kafizas, S. Skinner, D. J. Weiss, *J. Colloid Interface Sci.* **2020**, *580*, 834–849.
- [46] J. C. Bullen, C. Lapinee, P. Salaün, R. Vilar, D. J. Weiss, *J. Environ. Chem. Eng.* **2020**, *8*, 104033.
- [47] P. Ravenscroft, J. M. McArthur, B. A. Hoque, *Geochemical and Palaeohydrological Controls on Pollution of Groundwater by Arsenic*, Elsevier Science, **2001**.
- [48] P. K. Dutta, S. O. Pehkonen, V. K. Sharma, A. K. Ray, *Environ. Sci. Technol.* **2005**, *39*, 1827–1834.
- [49] M. Bissen, M. M. Vieillard-Baron, A. J. Schindelin, F. H. Frimmel, *Chemosphere* **2001**, *44*, 751–757.
- [50] M. A. Ferguson, M. R. Hoffmann, J. G. Hering, *Environ. Sci. Technol.* **2005**, *39*, 1880–1886.
- [51] S. Chi, C. Ji, S. Sun, H. Jiang, R. Qu, C. Sun, *Ind. Eng. Chem. Res.* **2016**, *55*, 12060–12067.
- [52] T. Xu, P. V. Kamat, K. E. O'Shea, *J. Phys. Chem. A* **2005**, *109*, 9070–9075.
- [53] R. A. Spurr, H. Myers, *Anal. Chem.* **1957**, *29*, 760–762.
- [54] T. Yamashita, P. Hayes, *Appl. Surf. Sci.* **2008**, *254*, 2441–2449.
- [55] J. H. Seinfeld, S. N. Pandis, *Atmospheric Chemistry and Physics: From Air Pollution to Climate Change*, Wiley-Blackwell, **2006**.
- [56] J. Tauc, *Mater. Res. Bull.* **1968**, *3*, 37–46.
- [57] I. Tunc, M. Bruns, H. Gliemann, M. Grunze, P. Koelsch, *Surf. Interface Anal.* **2010**, *42*, 835–841.
- [58] J. Zhang, P. Zhou, J. Liu, J. Yu, *Phys. Chem. Chem. Phys.* **2014**, *16*, 20382–20386.
- [59] M. Lira-Cantú, *The Future of Semiconductor Oxides in Next-Generation Solar Cells* **2017**.
- [60] D. O. Scanlon, C. W. Dunnill, J. Buckeridge, S. A. Shevlin, A. J. Logsdail, S. M. Woodley, C. R. A. Catlow, M. J. Powell, R. G. Palgrave, I. P. Parkin, G. W. Watson, T. W. Keal, P. Sherwood, A. Walsh, A. A. Sokol, *Nat. Mater.* **2013**, *12*, 798–801.
- [61] K. Sivula, F. Le Formal, M. Grätzel, *ChemSusChem* **2011**, *4*, 432–449.
- [62] X. Yong, M. A. Schoonen, *Am. Mineral.* **2000**, *85*, 543–556.
- [63] J. Low, J. Yu, M. Jaroniec, S. Wageh, A. A. Al-Ghamdi, *Adv. Mater.* **2017**, *29*, 1601694.
- [64] H. Wang, L. Zhang, Z. Chen, J. Hu, S. Li, Z. Wang, J. Liu, X. Wang, *Chem. Soc. Rev.* **2014**, *43*, 5234–5244.
- [65] S. Rtimi, C. Pulgarin, V. A. Nadtochenko, F. E. Gostev, I. V. Shelaev, J. Kiwi, E. Polytechnique, F. De Lausanne, C. Lausanne, *Sci. Rep.* **2016**, *6*, 2–11.
- [66] V. Vaiano, G. Iervolino, D. Sannino, L. Rizzo, G. Sarno, A. Farina, *Appl. Catal. B* **2014**, *160–161*, 247–253.
- [67] D. F. Ollis, *Front. Chem.* **2018**, *6*, 1–7.
- [68] B. Ohtani, *Adv. Inorg. Chem.* **2011**, pp. 395–430.
- [69] H. Haick, Y. Paz, *ChemPhysChem* **2003**, *4*, 617–620.
- [70] F. Amano, K. Nogami, M. Tanaka, B. Ohtani, *Langmuir* **2010**, *26*, 7174–7180.

- [71] E. O. Filatova, A. S. Konashuk, *J. Phys. Chem. C* **2015**, *119*, 20755–20761.
- [72] C. Daikopoulos, Y. Georgiou, A. B. Bourlinos, M. Baikousi, M. A. Karakasides, R. Zboril, T. A. Steriotis, Y. Deligiannakis, *Chem. Eng. J.* **2014**, *256*, 347–355.
- [73] A. Chauhan, M. Rastogi, P. Scheier, C. Bowen, R. V. Kumar, R. Vaish, *Appl. Phys. Rev.* **2018**, *5*, pp 1–26.
- [74] M. Zhang, C. Lai, B. Li, F. Xu, D. Huang, S. Liu, L. Qin, Y. Fu, X. Liu, H. Yi, Y. Zhang, J. He, L. Chen, *Chem. Eng. J.* **2020**, *396*, 125343.
- [75] C. Lai, Z. An, H. Yi, X. Huo, L. Qin, X. Liu, B. Li, M. Zhang, S. Liu, L. Li, Y. Fu, X. Zhou, Z. Wang, N. An, X. Shi, *J. Colloid Interface Sci.* **2021**, *600*, 161–173.
- [76] J. C. Bullen, A. Torres-huerta, P. Salaün, J. S. Watson, S. Majumdar, R. Vilar, D. J. Weiss, *Water Res.* **2020**, *175*, 115650.
- [77] J. A. Davis, J. A. Coston, D. B. Kent, C. C. Fuller, *Environ. Sci. Technol.* **1998**, *32*, 2820–2828.
- [78] J. Nelson, R. E. Chandler, *Coord. Chem. Rev.* **2004**, *248*, 1181–1194.
- [79] A. Cheng, R. Tyne, Y. T. Kwok, L. Rees, L. Craig, C. Lapinee, M. D'Arcy, D. J. Weiss, P. Salaün, *J. Chem. Educ.* **2016**, *93*, 1945–1950.
- [80] J. C. Bullen, L. Dworsky, M. Eikelboom, M. Carriere, A. Reiling, P. Salaun, *PLoS One* **2021**, *17*, e0262124.
- [81] H. F. Heiba, J. C. Bullen, A. Kafizas, C. Petit, S. J. Skinner, D. Weiss, *J. Photochem. Photobiol. A* **2022**, *424*, 113628.
- [82] C. Vallance, C. Vallance, *An Introd. to Chem. Kinet. Morgan And Claypool* **2017**.

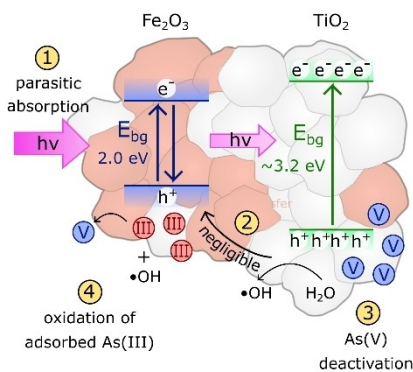
Manuscript received: November 21, 2021

Accepted manuscript online: February 3, 2022

Version of record online: ■■■, ■■■■

RESEARCH ARTICLE

The mechanisms that control the kinetics of arsenic(III) photocatalytic oxidation when meso-TiO₂ is coupled with an Fe₂O₃ adsorbent phase are investigated herein. Parasitic light absorption is the primary factor, followed by changes in rate law (from disguised zero-order to first order). Charge transfer across the heterojunction in our material is negligible.



Dr. J. C. Bullen*, H. F. Heiba, Dr. A. Kafizas, Prof. D. J. Weiss*

1 – 17

Parasitic Light Absorption, Rate Laws and Heterojunctions in the Photocatalytic Oxidation of Arsenic(III) Using Composite TiO₂/Fe₂O₃

